LLNL-JRNL-2014890

Lawrence Livermore National Laboratory

Characterizing Microscale Signatures in Uranium Ore Concentrates Using Electron Probe Microanalyzer

C Chan, J Boro, A Gaffney, N Marks, R Lindvall, J Swider

April 2026

Journal of Radioanalytical and Nuclear Chemistry

Disclaimer

This work performed under the auspices of the U.S. Department of Energy by Lawrence Livermore National Laboratory under Contract DE-AC52-07NA27344.

Title page

Names of the authors: Christine F. Chan[1*], Joseph R. Boro[1], Amy M. Gaffney[1], Naomi E. Marks[1], Rachel E. Lindvall[1], Joseph R. Swider[1]

Title: Characterizing Microscale Signatures in Uranium Ore Concentrates Using Electron Probe Microanalyzer

Affiliation(s) and address(es) of the author(s): [1]Nuclear and Chemical Sciences Division, Lawrence Livermore National Laboratory, 7000 East Avenue, Livermore, CA 94550, USA

E-mail address of the corresponding author: chan67@llnl.gov

Characterizing Microscale Signatures in Uranium Ore Concentrates Using Electron Probe Microanalyzer

Christine F. Chan[1*], Joseph R. Boro[1], Amy M. Gaffney[1], Naomi E. Marks[1], Rachel E., Lindvall[1], Joseph R. Swider[1]

[1]*Nuclear and Chemical Sciences Division, Lawrence Livermore National Laboratory, 7000 East Avenue, Livermore, CA 94550, USA*

Abstract

Impurities in uranium ore concentrates (UOCs) serve as forensic signatures of processing history and origin. This study utilizes Electron Probe Microanalyzer (EPMA) to characterize microscale compositional and textural features in individual UOC particles from both commercial and bench-scale production. At the particle scale, multiple internal phases with distinct morphologies, chemical signatures, and stoichiometries are documented. Our data shows that chemical impurities are heterogeneously distributed within single particles and among particles within a sample. These microscale heterogeneities correlate with known processing histories, indicating that microscale signatures of early fuel cycle materials can provide valuable information for nuclear forensic material analysis.

Keywords

Uranium ore concentrate; nuclear forensics; Electron Probe Microanalyzer; microscopy; principal component analysis

Introduction

The science of nuclear forensics aims to establish and validate approaches to discern the history and origin of unknown nuclear materials, addressing questions relevant to specific forensic investigations or broader nuclear security concerns. At its core are "signatures"—measurable properties such as isotopic composition, elemental concentrations, and physical or chemical characteristics—that singly or together connect materials to their origin, intended use, production history, and processing methods [1]. The diverse range of materials, production methods, and process conditions utilized throughout the nuclear fuel cycle has the potential to produce a vast array of signatures that may be evident in nuclear fuel cycle materials [2, 3]. Effective use of signatures depends on two core components: the ability to generate accurate data using appropriate analytical techniques, and the ability to interpret these measurements to reveal specific aspects of a sample's history or provenance. To verify the utility of specific nuclear forensics signatures, it is necessary to validate them in materials with well-documented origins and processing histories. One aspect of this process involves investigating the spatial scale of a particular signature—exploring the expression of a signature with microanalytical as well as bulk analysis methods to establish and validate the signature at a range of spatial and physical scales.

The spatial scale at which a material is analyzed is fundamentally context dependent and spans a continuum from microanalytical to bulk analysis methods. Bulk analyses typically require macroscopic quantities of material, on the order of 10 micrograms or more, and often involve homogenization through processes like digestion. In contrast, microanalytical techniques interrogate much smaller amounts of material, from individual particles to micrometer to millimeter scale fragments. Determining the specificity and spatial scale of a particular signature, whether it manifests in individual particles or sample fragments, in bulk material, or across multiple scales, is critical for signature discovery and validation and proper interpretation of a nuclear material's history. Recent advancements in analytical instrumentation and methodologies allow researchers to address increasingly complex questions how bulk and spatially resolved microanalytical data record production history. These developments highlight the importance of integrating complementary analytical approaches into nuclear forensics material analysis campaigns. Electron Probe MicroAnalysis (EPMA), despite its widespread use in the

Earth sciences and material sciences [4, 5], remains largely underutilized in nuclear forensics [6–8], representing a significant opportunity to advance the field.

Uranium ore concentrates (UOC) present an ideal test case for evaluating EPMA's potential utility in nuclear forensic material analysis. These early fuel cycle materials, containing approximately 60–80% uranium and produced worldwide in large quantities, are vulnerable to trafficking. Various processing methods are used to manufacture UOCs, resulting in different chemical forms such as triuanium octoxide, uranyl hydroxide, uranyl peroxide, ammonium diuranate (ADU), and sodium diuranate, each with distinctive physical and chemical properties that reflect their production history [3]. Previous studies using bulk material data have demonstrated that composition and particle morphology can serve as signatures for different UOC production processes and origins [9–16]. However, typical UOC characterization workflows rely on bulk analytical approaches to provide averaged compositional information across an entire analytical aliquot, which may range from 0.25 g to greater than 1 g [9, 10, 16–24]. The diverse production scales and varied processing methods employed in UOC manufacturing likely create a wide spectrum of microscale characteristics in UOC particles, offering significant potential for development as new forensic signatures [25–33]. Despite this potential, the specific manifestation of bulk characteristics at the microscale within UOCs remains largely unexplored.

In this study, we document the spatial scale of heterogeneities in UOCs and correlate microstructure and microscale characteristics with bulk compositional characteristics. Using EPMA, we will describe the chemical composition of solid materials at sub-micrometer scale, addressing the following questions:

1. **What is the spatial scale of heterogeneity in UOCs?**
   We seek to determine whether heterogeneity is primarily found at the single-particle level or within sub-particle structures. Understanding the spatial distribution and scale of heterogeneity will clarify how processing methods impart micro-signatures to UOCs.
2. **Are there microscale characteristics unique to each UOC sample that are indicative of material type and production methods?**

92 We investigate whether EPMA can reveal chemical and textural features at the
93 microscale that indicate heterogeneity in UOC samples that is not evident at
94 the bulk scale. This would enable the development of new signatures of
95 specific UOC production processes and provide a new capability for nuclear
96 forensic material analysis.

97 # Experimental

98 ## Investigated samples and processing history

99 We selected four UOC samples with well constrained provenance and processing
100 histories that represent a range of chemical processing approaches (Table 1). Two UOCs
101 were collected from commercial plant-scale production facilities, and a paired set of
102 samples was produced under highly controlled bench-scale conditions in a research
103 laboratory.

104 **Table 1** Uranium ore concentrate sample descriptions, including geologic deposit,
105 summary of its processing history and crystallographic phases. XRD—X-ray diffraction

Sample Name	Origin	Type of geologic deposit	Processing history	Crystallographic phases determined by XRD
Commercial $UO_4 \cdot 4H_2O$	United States	Fault-controlled roll-front	Extracted by in-situ recovery; purified by ion-exchange columns, no calcination	$UO_4 \cdot 4H_2O$ + $2HNO_3$
Commercial ADU	South Africa	Quartz-pebble conglomerates	Leached in sulfuric acid; purified by ion-exchange columns and solvent extraction	$U_3(NH_3)O_9 \cdot 5H_2O$ Uranium Ammine Oxide Hydrate; $(UO_2)_3(SO_4)_2(OH)_2 \cdot 8H_2O$ Zippeite
Bench-scale UO_4	Oak Ridge National Laboratory	---	Precipitated from the uranyl nitrate solution using hydrogen peroxide	$(UO_2)(O_2)(H_2O)_2$ Metastudtite
Bench-scale UO_2	Oak Ridge National Laboratory	---	Calcination product of the bench-scale UO4	UO_2; UO_2-$2H_2O$ minor schoepite

Commercial UOCs

The commercial $UO_4 \bullet 4H_2O$ sample is a uranium peroxide product derived from a uranium ore deposit in the United States (Table 1). Uranium mineralization at this deposit occurs in fault-controlled roll-fronts within fluvial sandstones and is extracted by in-situ recovery methods. The leached uranium is purified using ion-exchange columns and eluted from the resin with sodium carbonate. The uranium is subsequently precipitated, filtered, and dried to yield the final UO_4 product.

The commercial ADU sample originates from a uranium ore mined in South Africa (Table 1). At this deposit, uranium is hosted in quartz-pebble conglomerates and extracted using conventional hard-rock techniques. The crushed ore is leached with concentrated sulfuric acid, and the extracted U is then purified using ion-exchange columns and solvent extraction with tri-octyl/dodecyl amine. The product is then precipitated, filtered and dried to produce ADU.

Paired bench-scale UOCs

A paired set of uranium oxides were synthesized at the bench-scale (100-g scale) at Oak Ridge National Laboratory. The starting material was natural triuranium octoxide, which was dissolved using nitric acid to form a uranyl nitrate solution. The bench-scale UO_4 is a uranium peroxide hydrate (Table 1) that was precipitated from the uranyl nitrate solution using hydrogen peroxide. The bench-scale UO_4 was calcined in a Hastelloy reactor at 550 °C for seven hours under a mixed H_2 and N_2 atmosphere, resulting in the production of uranium dioxide (bench-scale UO_2).

Methods

Sample Preparation for Particle Mounts

The UOC particles were dispersed onto a silicon wafer for initial scanning electron microscopy-energy dispersive X-ray spectroscopy (SEM-EDS) screening using a slurry of UOC powder and Vetrel XF solvent (TMC Industries' proprietary hydrofluorocarbon

fluid). Vertrel XF, with its low viscosity (0.67 cP), high density (1.58 kg/L), and low surface tension (0.0141 N/m), enables rapid drying and minimizes particle clumping compared to common alcohols like methanol or isopropyl alcohol. To maximize particle separation, the sample and solvent mixture was sonicated for at least 15 minutes. The dispersed sample was then incrementally dispensed onto the wafer using a 20 µL pipette.

Sample Preparation for Particle Cross-Sections

Polished particle mounts were prepared using the PELCO Eponate 12^{TM}-Araldite 502 Kit with DMP-30. The epoxy was pre-mixed in 5 mL aliquots and stored frozen until use, then thawed at 70 ºC before embedding. A small amount of UOC powder was placed in a silicone epoxy mold, and the heated epoxy was poured over it and gently stirred for even distribution. The mounts were cured at 70 ºC for 12–18 hours, then polished with diamond lapping paper and diamond paste on a polishing cloth. Smaller particles and fragments (< 10 µm) are likely removed during sample polishing.

Scanning Electron Microscopy

Initial sample characterization was performed at Lawrence Livermore National Laboratory (LLNL) using a TESCAN MIRA3 SEM equipped with an EDAX EDS detector. Imaging and EDS analyses were conducted at 13–15 keV beam energy and a 15 mm working distance, with EDS spectra acquired for 60 seconds. Data collected from the silicon wafer mounts were used to identify key elements for subsequent EPMA analysis and assist in characterizing internal phases within the polished epoxy mounts.

Electron Probe Micro Analysis

Quantitative spot analyses and elemental mapping of polished UOC epoxy mounts were performed at LLNL on a JEOL JXA-8530F field-emission Hyperprobe equipped with five wavelength-dispersive spectrometers (WDS). Complete spot-analysis data, including critical detection limits (CDLs), counting-statistics errors, and standards data are reported in the Supplementary Tables 1–2. CDLs at 99% confidence were calculated

from the measured background count rate and the analytical sensitivity determined from calibration standards analyzed before data collection.

Spot analyses were acquired at 15 keV and 10 nA with a 3 μm beam and 90 s on-peak counting. Time-dependent intensity (TDI) corrections were applied to mitigate beam-induced drift in the UOC matrix **[34, 35]**. We measured eight to ten spots on roughly ten particles per sample, for a total of roughly 80 to 100 analyses per sample. Based on ICP-MS data for the UOC samples, ten elements with bulk concentrations greater than 100 ppm were selected for EPMA analysis: Na, Mg, Al, S, Ca, Zr, Fe, Mo, Ti, and Cr. Backgrounds were treated with the mean atomic number (MAN) method and totals were evaluated using formula-by-difference where appropriate [36–38]. In the MAN approach, the continuum background beneath each analyte peak is predicted from a calibration of background intensity versus mean atomic number built from standards (Supplementary Table 2). This allows longer on-peak counting with no point-by-point off-peak measurements, which lowers detection limits for a given analysis time. The bulk stoichiometry of each sample was independently constrained by powder X-ray diffraction (XRD) analysis (Table 1).

Elemental maps were collected at 15 keV and 20 nA with a dwell time of 300 ms per pixel. Current and dwell settings were selected to balance X-ray statistics and minimize damage to the uranium matrix. Mapping focused on elements present at higher concentrations in the spot data (Na, S, Ca, Ti, Fe). Although TDI methods for mapping are available **[38]**, a single mapping pass was used here.

Inductively Coupled Plasma Mass Spectrometry

Four aliquots of each of the two commercial UOCs were dissolved in HNO_3 with trace HF and analyzed for minor and trace element analysis by high resolution inductively coupled plasma mass spectrometry (HR-ICP-MS) on an Thermo Scientific Element 2 XR. These solutions were diluted in triplicate to 100 μg U/g solution. The dilutions were made in an internal standard solution of 1 ppb Rh to determine corrections for instrument drift. Quantitative analysis was performed using a linear calibration curve based on certified multi-element external standards in a matching uranium matrix. The

certified reference material "Morille" (CETAMA) was digested separately and run as QA/QC.

The average of the three preparations is calculated, and the reported uncertainty is the average of the combined standard uncertainty of the three preparation results in addition to the standard deviation of the three separate results with a coverage factor of k = 2, representing a confidence interval (CI) of approximately 95% (Table S3). All reported uncertainties incorporate statistical and systematic components. A decision limit (L_c) was calculated as the standard deviation of the analytical results of three separate preparations of the process blank for each sample, multiplied by a coverage factor, k. The decision limit was calculated at the 99% CI (k = 9.925, two-tailed t-statistic for n = 3) and is reported as μg/g sample.

X-ray diffraction

For the bench-scale UOCs, XRD analysis was performed using a Rigaku SmartLab XE X-ray diffractometer equipped with a HyPix 3000 detector. Data acquisition was performed using the Rigaku SmartLab Studio II software package. Each sample was mounted as received onto a silicon zero-background holder featuring a 0.1 mm deep well. The powder was leveled with the top of the well using a glass slide. To prevent contamination, each holder was covered with a PMMA dome. Additionally, a silicon X-ray Standard Reference Material (SRM 640f, NIST) was analyzed. The scanning parameters were set to a range of 10 to 100° 2θ, with a step size of 1°/min, utilizing a Ni-filtered Cu X-ray beam generated from a rotating anode operating at 45 kV and 200 mA. The standard pattern exhibited a deviation of less than 0.1° from the expected standard peaks, which is acceptable for accurate pattern matching. The phases present in the samples were identified by comparing the observed peaks against the data in the International Centre for Diffraction Data (ICDD PDF-5+ 2025) powder diffraction database, using MDI JADE XRD analysis software.

For the commercial UOCs, XRD analysis was performed using a Bruker AXS D8 ADVANCE X-ray diffractometer equipped with a LynxEye 1-dimentional linear Si strip detector. Bruker DIFFRAC.EVA V3.1 was used for data analysis. The sample was placed onto a frontload poly methyl methacrylate (PMMA) sample holder with dome. The

scanning parameters were set to a range of 10 to 70° 2θ. The step scan parameters were 0.02° step and 4 second counting time per step with a 12mm variable divergence slit. The samples were X-rayed with Ni-filter Cu radiation from a sealed tube operated at 40kV and 40mA. An X-ray reference material (Bruker supplied Al_2O_3) was analyzed with the sample to ensure goniometer alignment. Phases in the unknown sample were identified by comparison of observed peaks to those in the International Centre for Diffraction Data (ICDD PDF-2 2009 and PDF-4+ 2013) powder diffraction databases.

Results

In this study, a "particle*"* is defined as an individual, discrete solid grain of UOC, typically 10–500 μm in size and suitable for EPMA analysis. Particles contain one or more "phases," where a "phase" is a region with distinct texture and/or chemical composition. Some particles contain an "inclusion," defined as a texturally distinct, coherent region within a particle that is noticeably different from the host matrix and comprises its own phases. Inclusions and internal phases are observed only in particle cross-sections viewed with EPMA-BSE imagery.

Morphological Assessment of Bulk Material

Morphology descriptions for the UOC samples as based on the lexicon of Tamasi et al. [39]. Each UOC sample has a distinct but uniform particle morphology (Fig. 1; Table 1). The commercial ADU sample occur as polydisperse particles with surficial cracking. The commercial $UO_4 \bullet 4H_2O$ and bench-scale UO_4 samples occur as agglomerative particles though the commercial $UO_4 \bullet 4H_2O$ sample also contains polydisperse particles. The agglomerate's finer grains display diverse morphologies: reticulated in the commercial $UO_4 \bullet 4H_2O$, globular and reticulated grains in the bench-scale UO_4, and platy in the bench-scale UO_2 (Fig. 1).

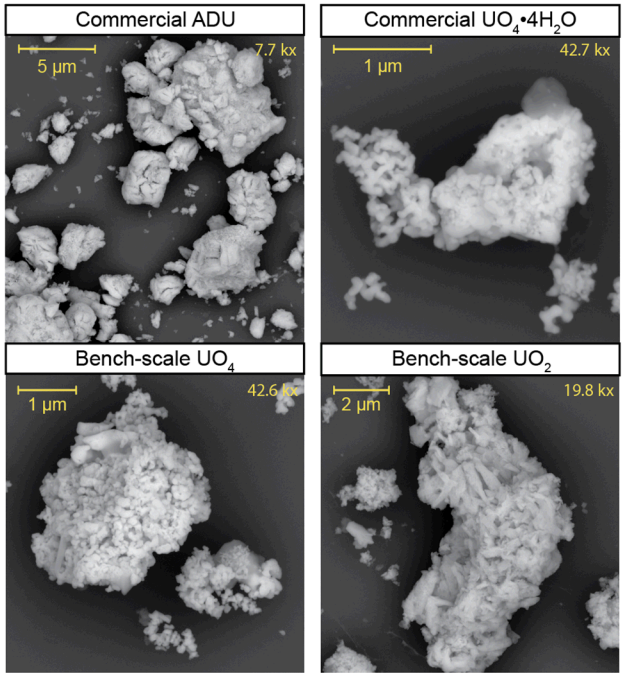

Fig. 1 Particle morphologies of UOC samples from SEM-BSE imagery. Except for the commercial ADU sample, all samples occur as agglomerative particles. The commercial ADU and portions of commercial UO_4•$4H_2O$ also occur as isolated, polydisperse single particles

EPMA Phase Characterization

Analysis of polished sections of single polydisperse particles by EPMA reveals multiple internal phases, distinguished by variations in texture, BSE brightness, and chemical composition. BSE brightness corresponds to the mean atomic number of a material, with regions containing higher-atomic-number elements appearing brighter. Differences in BSE brightness are primarily controlled by variations in uranium concentration relative to oxide stoichiometry, such as the presence of oxygen, hydroxide, and water in the crystal structure. Using the EPMA spot analyses and quantitative maps, we demonstrate that chemical heterogeneity exists at the sub-particle scale in the UOC samples (Figs. 6–9, S1–S4).

In the commercial ADU sample, three distinct internal phases were identified: (1) a groundmass matrix, (2) a high-uranium phase with high BSE brightness, and (3) a high-

sulfur phase with irregular morphology and moderate BSE brightness (Fig. 2). Elements such as S, Ca, and to a lesser degree, Fe and Ti, are concentrated in the non-groundmass phases (Figs. 6 and S1). The high-sulfur phase exhibits elevated concentrations of S (>1.6 wt.%), Ca (>0.12 wt.%), and slightly higher Ti (~0.12 wt.%), compared to the groundmass (Fig. 6). The high-uranium phase is characterized by elevated Ti ($\geq$ 0.18 wt.%) and lower S (<0.4 wt.%) compared to the high-sulfur phase. Elements such as Na are distributed more evenly throughout the particles.

In the commercial $UO_4 \bullet 4H_2O$ particles, the most common phases include: (1) a high-sulfur phase that has a subrounded morphology, extensive internal fracturing and moderate BSE brightness, (2) a high-uranium phase characterized by rounded morphology and high BSE brightness, and (3) groundmass matrix (Fig. 3). Some particles contain compositionally distinct inclusions (Fig. 3d). The high-sulfur phases show > 0.12 wt. % S, which is significantly higher than the groundmass (< 0.1 wt. %; Figs. 7 and S2). One inclusion within the particle (Figs. 3 and 7) exhibits significantly higher concentrations of Na (> 0.35 wt. %) and Ca (~0.23 wt. %). The distribution of other elements mapped is relatively uniform across the particles and phase types. The high-uranium phase is not chemically distinct in terms of the elements analyzed by EPMA (Fig. 7).

In the bench-scale UO_4 sample, the two most common phases are: (1) groundmass matrix, and (2) high-sulfur phase with moderate BSE brightness. However, many particles also contain BSE-bright inclusions (Figs. 4 and 8). The high-sulfur phase (Figs. 8 and S3) exhibits elevated S content ($\geq$ 1.7 wt.%) and is occasionally associated with elevated Ti ($\geq$ 0.06 wt.%). Sulfur in the is slightly higher ($\geq$ 0.2 wt.%) in the inclusion relative to the groundmass ($\leq$ 0.1 wt.%) but lower than the high-sulfur phase. Some bench-scale UO_4 particles display rims enriched in Fe, S, and Na (Fig. S3).

In the bench-scale UO_2 sample, the main phases observed are: (1) crystal-lath phase with high BSE brightness (Fig. 5c–5d), (2) a groundmass matrix, (3) an accreted conglomerate phase composed smaller fragments with variable BSE brightness and minor interstitial matrix (Fig. 5A), and (4) a high-uranium phase with high BSE brightness. The

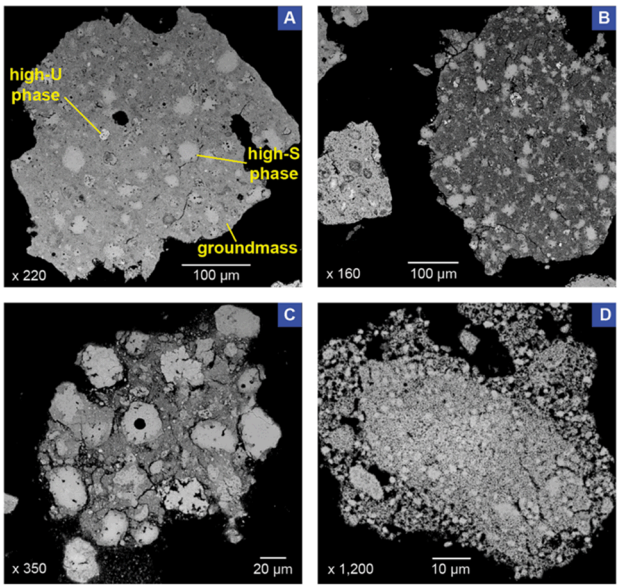

287

288 **Fig. 2** BSE cross-sectional views of commercial ADU particles collected by EPMA.
289 There are at least three distinct phases: (1) groundmass matrix, (2) high-uranium phase
290 with high BSE brightness, and (3) high-sulfur phase. BSE brightness can vary in the
291 groundmass as seen in panel B

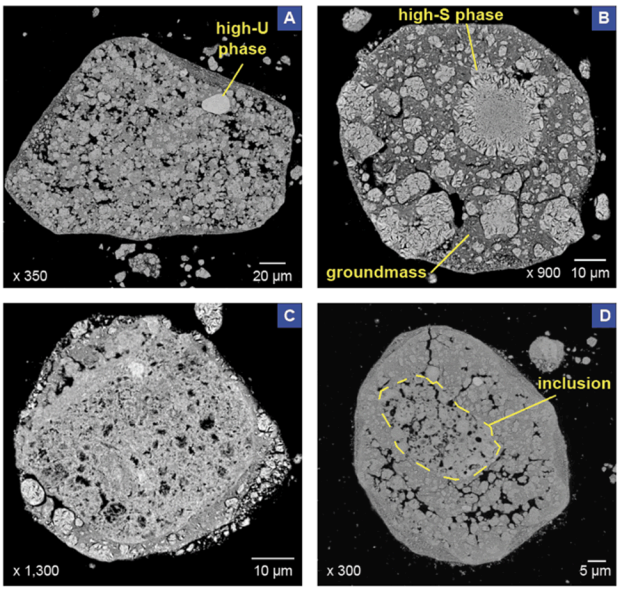

292

293 **Fig. 3** BSE cross-sectional views of commercial UO_4•$4H_2O$ particles collected by
294 EPMA. There are at least three distinct phases: (1) a high-sulfur phase with extensive
295 internal fracturing, (2) high-uranium phase with high BSE brightness, and (3)
296 groundmass matrix

297

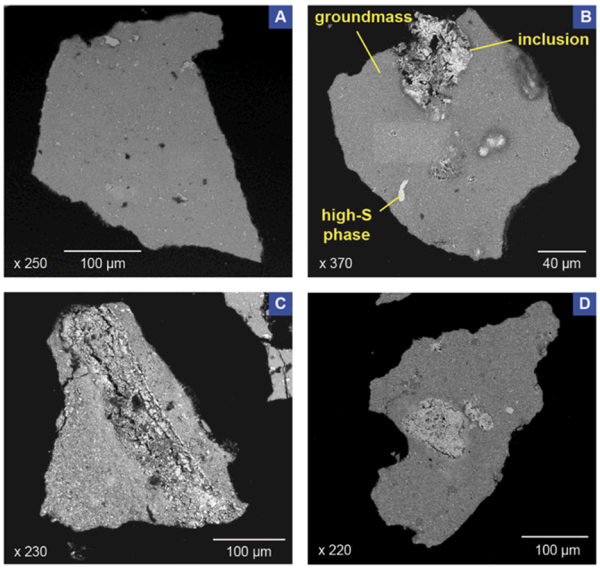

Fig. 4 BSE cross-sectional views of bench-scale UO_4 particles collected by EPMA. There are at least two distinct phases: (1) groundmass matrix and (2) a high-sulfur phase. Inclusions are common in these particles. The light gray rectangle in panel B is an artifact of the analysis

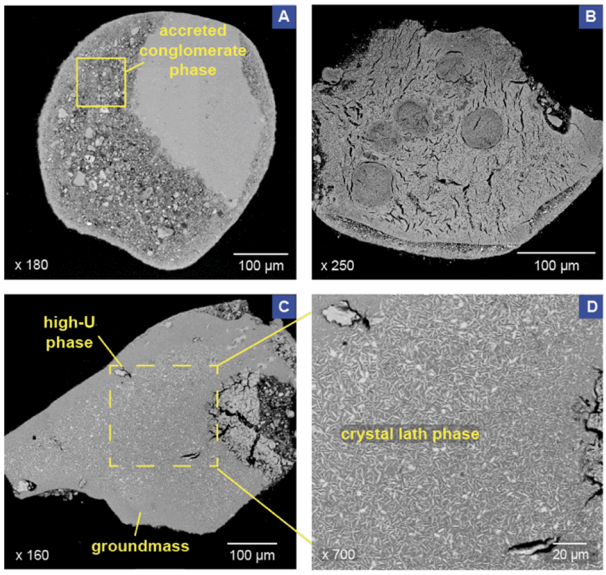

Fig. 5 BSE cross-sectional views of bench-scale UO_2 particles collected by EPMA. Panel D is a close-up of the acicular, crystal-lath phase highlighted in the dashed yellow box in panel C. There are at least four distinct phases: (1) crystal lath phase, (2) groundmass matrix, (3) high-uranium phase and (4) conglomerate phase

conglomerate phase is compositionally diverse and typically enriched in transition metals such as Cr, Ni and Mo. Both the crystal-lath and high-uranium phases are compositionally indistinguishable from the groundmass (Fig. 9). Their differences are seen in BSE brightness, which, based on SEM-EDS characterization, likely reflect variability in the uranium content and hydration level.

Principal component analysis

The EPMA results highlight that UOC particles exhibit internal morphological and textural heterogeneities at the sub-particle level for both bench-scale and plant-scale UOCs. To better examine major compositional trends among the identified phases and individual particles, we performed principal component analysis (PCA) on EPMA spot analyses (Table S1). We also explored several unsupervised clustering algorithms (e.g., density-based spatial clustering, hierarchical clustering, k-means) as well as a supervised clustering algorithm (e.g., support vector machine). However, due to the relatively low variance between samples and particles, as well as the small dataset size, these clustering algorithms struggled to accurately identify an appropriate number of clusters or to match clusters with our textural classifications from BSE imagery. Therefore, we focus on the PCA results below.

To ensure statistical robustness in the PCA analysis, only variables detected in approximately 20% of the total analyses above the CDL were included. This threshold was chosen to balance statistical reliability with the goal of maximizing the number of variables and is consistent with practices in similar studies [40]. Including variables with a high proportion of values below the CDL can distort PCA results and reduce interpretability; thus, this approach helps ensure that the principal components reflect genuine compositional variability rather than artifacts from sparsely detected variables. The selection process ensured that at least five variables were retained for PCA, except for bench-scale UO_4 where only three variables met the 20% threshold. When two variables were found to be highly correlated in PCA space, one was excluded to reduce redundancy and prevent disproportionate influence on lower-order principal components.

Prior to PCA, data were standardized using Z-score normalization so that each variable had a mean of 0 and a standard deviation of 1.

It is important to note that some degree of user bias may be present in the selection of analytical spots, as choices may be influenced by visible features or perceived heterogeneity within the sample. This could potentially affect the representativeness of the dataset and, consequently, influence the PCA results by over- or under-representing certain compositional domains. Efforts were made to select spots as objectively as possible, but the possibility of sampling bias cannot be fully excluded. Biplots summarizing the PCA results are presented in Figures 10–11 and in the supplementary materials (Figs. S5–S8).

Chemical heterogeneity in commercial $UO_4 \bullet 4H_2O$ particles

The PCA of commercial $UO_4 \bullet 4H_2O$ particles were based on six variables: Na, Mg, S, Ca, Ti, and Cr. We chose to exclude Fe, despite meeting the criteria for PCA, because Fe and Ti were highly correlated. Three principal components (PCs) explained 78% of the total variance (Figs. 10 and S5). The groundmass and high-sulfur phases are clearly separated by non-colinear S and Na eigenvectors (Fig. 10a). Assessment of the high-uranium phase is limited due to its lower abundance and fewer EPMA analyses, but it generally falls between the two main phases. Variability within each phase is largely driven by Ca, Ti, Cr, and Mg. At the particle level, distinct compositional separation is evident among particles in PCA space, particularly between particles 1, 5, and 6, with these inter-particle differences strongly correlated to S and Na content (Figs. 10b). The eigenvectors governing intra-particle variability differ between the individual UO_4 particles.

Chemical heterogeneity in commercial ADU particles

For the commercial ADU particles, five variables (Na, S, Ca, Mo, and Ti) were selected for PCA. Three PCs accounted for 87% of total variance (Fig. S6). The analysis reveals clear separation between the groundmass and high-sulfur phases along PC1 eigenvectors (Ca, Mo, and S; Fig. S6A). Variability in the groundmass is predominantly

365 **Fig. 6** EPMA quantitative elemental maps for a commercial ADU particle, with weight
366 percent represented as a heat map. The bottom right panel displays a BSE image with
367 major phases labeled

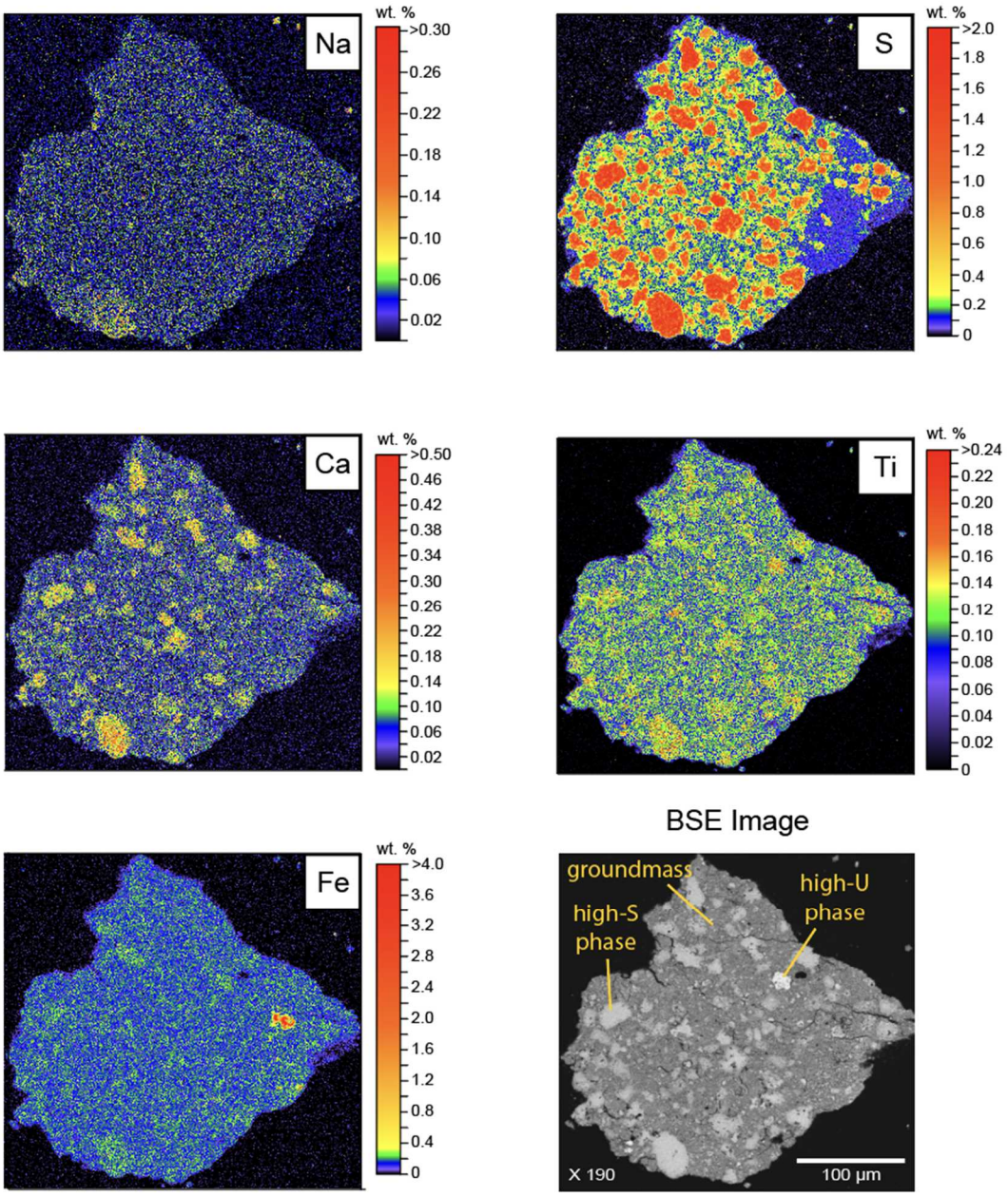

368

369

370 **Fig. 7** EPMA quantitative elemental maps for a commercial $UO_4 \cdot 4H_2O$ particle, with
371 weight percent represented as a heat map. The bottom right panel displays a BSE image
372 with the phases labeled

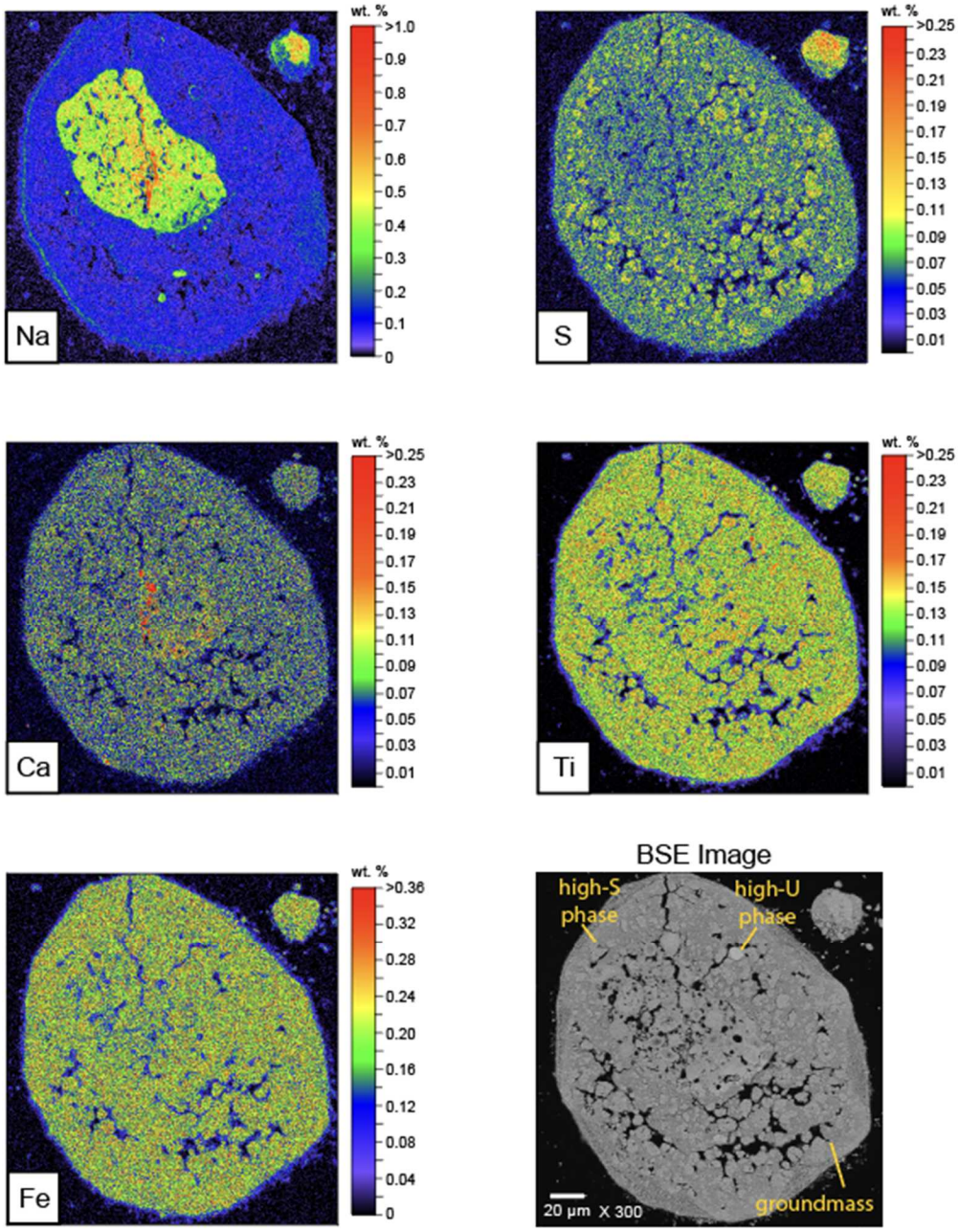

373

374 **Fig. 8** EPMA quantitative elemental maps for a bench-scale UO_4 particle, with weight
375 percent represented as a heat map. The bottom right panel displays a BSE image with the
376 phases labeled

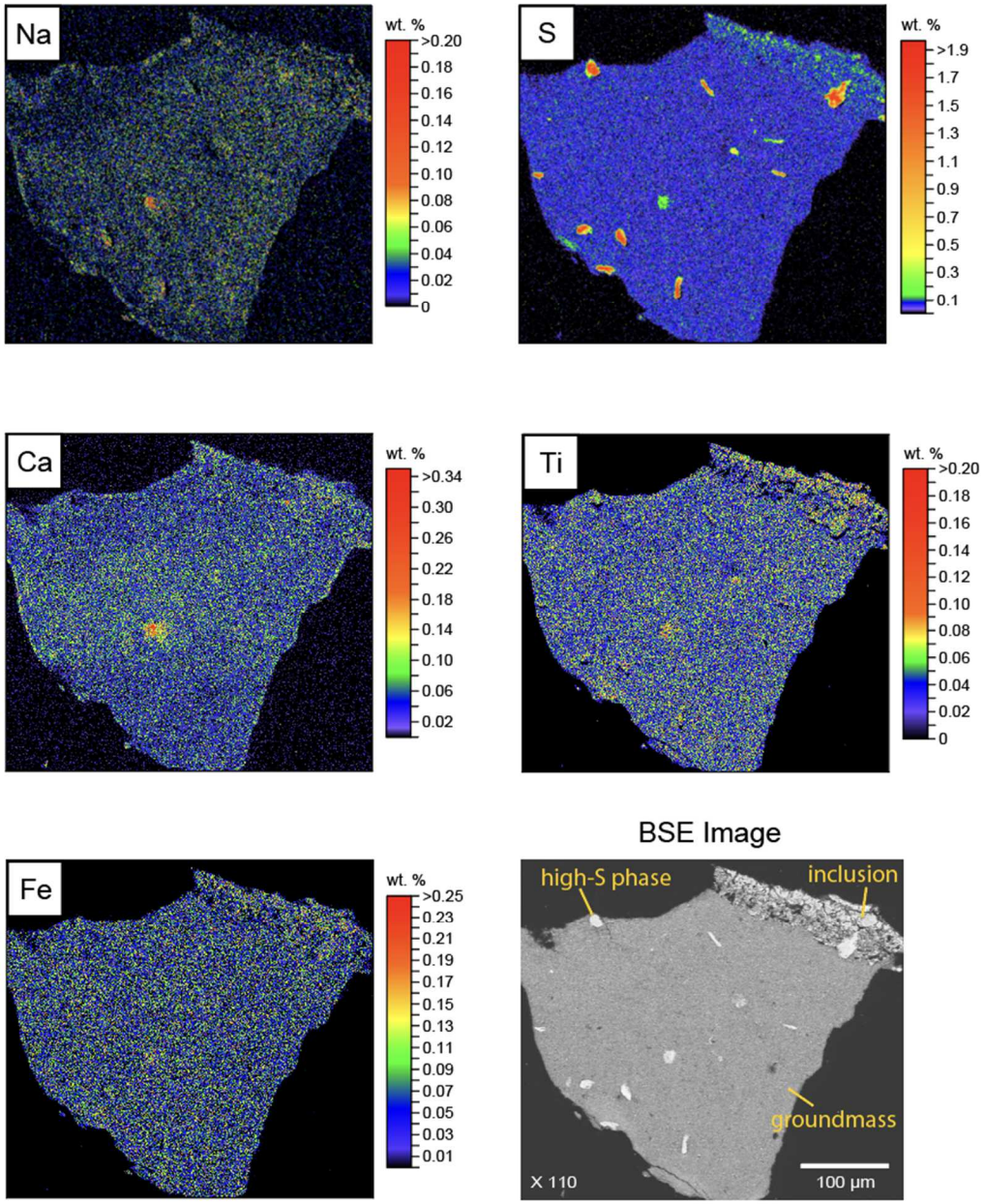

377

378

Fig. 9 EPMA quantitative elemental maps for a bench-scale UO_2 particle, with weight percent represented as a heat map. The bottom right panel displays a BSE image with some of the phases labeled

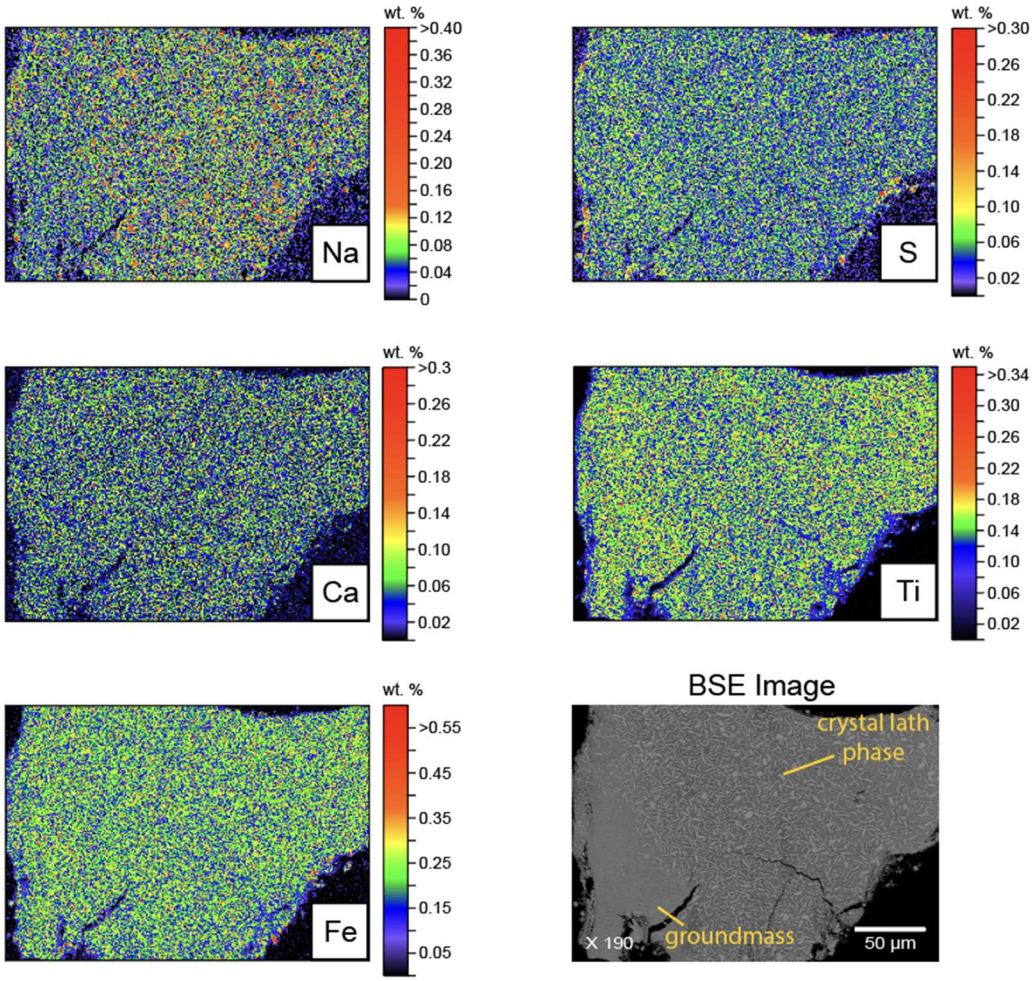

influenced by PC2 eigenvectors (Na and Ti) while the high-uranium phase is influenced by both principal components. When PCA results are grouped by individual particles (Fig. S6c), there is no distinct separation between particles in PCA space; however, internal variability within each particle is driven by different eigenvectors. For example, particle 12 is primarily influenced by PC2 eigenvectors, whereas variability in particle 9 is more driven by PC1 eigenvectors.

Chemical heterogeneity in bench-scale UO_4 particles

For bench-scale UO_4 particles, PCA was performed on three variables: Na, Ca, and S. Two PCs accounted for 84% of the total variance (Fig. S7). The groundmass and inclusions show substantial overlap in PCA space, with minor variability in all three elements. In contrast, variability specific to the high-sulfur phase is mainly influenced by S. Notably, Mo concentrations exceeded the CDL in 7% of all analyses though fell below the criteria to include in the PCA analysis. PCA analysis by particle ID indicates that some particles, such as 24 and 27, are relatively homogeneous, while others, including 26, 28, and 31, exhibit greater compositional variability (Fig. S7b).

Chemical heterogeneity in bench-scale UO_2 particles

The PCA of bench-scale UO_2 particles was performed using five variables: Na, S, Mo, Cr and Fe. Three principal components accounted for 85% of the total variance (Fig. S8). The groundmass and bright phases exhibit significant overlap in PC1 vs. PC2 space, with internal variability primarily controlled by Na and S. The conglomerate phase shows the greatest internal variability, driven largely by Na and S, but also includes a small number of high leverage analyses that are compositionally extreme in trace metals (Mo, Cr, Fe), reaching from several weight percent up to about 25 wt. %. The lath phase was excluded due to its lack of chemical distinction from the groundmass in the EPMA quantitative map and its size being insufficient for spot analysis (Fig. 4). Notably, only some particles (particles 19 and 20) contain the conglomerate phase, indicating most of the observed heterogeneity is driven by these few particles (Fig. S8c).

Comparative analysis between all UOC samples

To evaluate the distinctiveness of the elemental compositions for each UOC sample, PCA was conducted on all four UOC samples using five variables measured by EPMA: Na, Ca, S, Ti, and Mo (Fig. 11). Both Fe and Cr were excluded from the analysis due to their strong correlation with Mo. The first two PCs accounted for 65% of the total variance. In the PC1 vs. PC2 plot, the two commercial UOC samples were clearly differentiated from the other three samples, primarily by variations in Ca, S, Na, and Ti. In contrast, the two bench-scale samples show significant overlap, which is expected

Fig. 10 PC1 versus PC2 plots of the commercial $UO_4•4H_2O$ sample. A total of 90 spot analyses from seven particles were included. (A) Data are categorized based on phases identified by EPMA-BSE imagery (see inset image). (B) Data are categorized based on which particle the analysis came from. Biplot lines are exaggerated by a factor of 2 to better illustrate the contribution of the variable for a particular PC. The explained variance for each PC is shown in paratheses of the figure axis

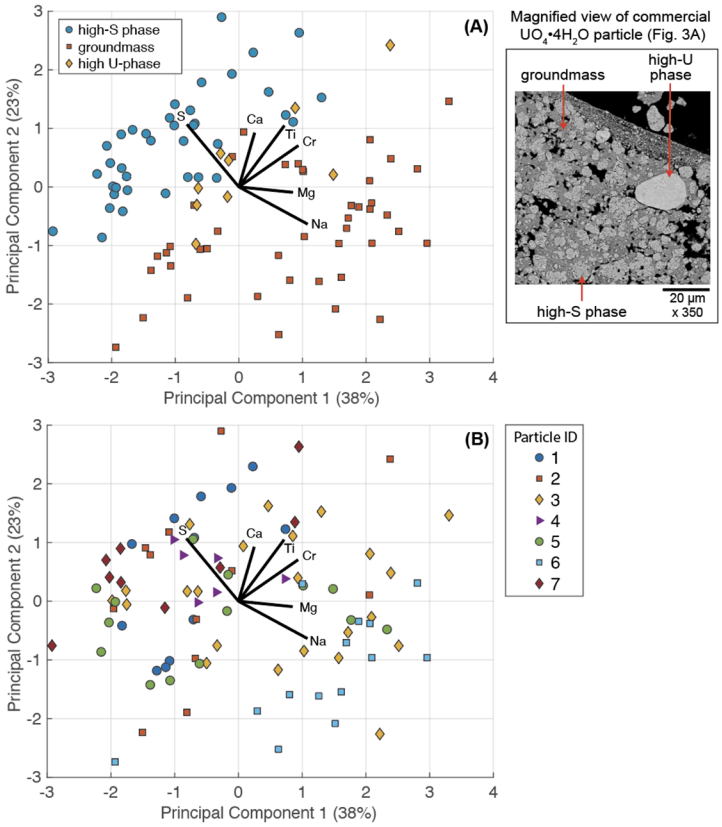

given their intrinsic relationship. Some variability in bench-scale UO_2 particles was associated with Mo, a contaminant likely introduced during the calcination of bench-scale UO_4. The principal components 3 and 4 contributed an additional 28% of the variance and revealed sample-specific trends (Fig. 11). Aside from the bench-scale UO_2, which is distinguished from the other samples by Mo content, internal variability for each sample is driven by the other variables.

Fig. 11 PCA plots including all four UOC samples. (A) PC1 versus PC2 illustrating variability between UOC samples and (B) PC3 versus PC4 illustrating sample-specific variability. Biplot lines are exaggerated by a factor of 4 to better illustrate the contribution of the variable for a particular PC

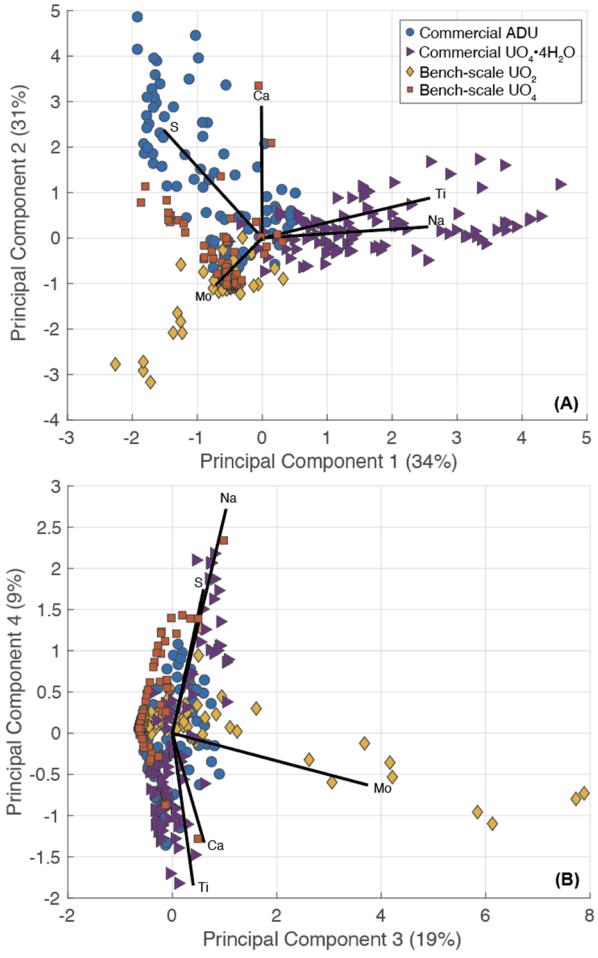

Discussion

Microscale heterogeneities in early fuel cycle materials

Our EPMA data reveal significant microscale heterogeneities in early fuel cycle materials. While each UOC sample exhibits a distinct yet internally uniform particle morphology (Fig. 1; [30, 41–43]), their internal structures are compositionally and texturally heterogeneous. We observe distinct phases within individual UOC particles

that correlate with notable elemental variability (Figs. 6–10; Figs. S1–S4). For example, phases in commercial ADU have S and Fe concentrations that differ by several weight percent (Fig. 6). Similarly, the range of Na contents in commercial $UO_4 \bullet 4H_2O$ phases spans a few weight percent. Additionally, the EPMA data also reveal compositional disparities between particles within the same sample (e.g., particle 1 vs. particle 6 in Fig. 10b), indicating differential incorporation of impurities during formation. The EPMA quantitative maps show that microscale heterogeneity exists on the several micron scale.

Uranium distribution within UOC particles is also heterogeneous, as evidenced by variations in backscattered electron (BSE) brightness. Higher BSE brightness correlates with higher uranium content relative to oxide stoichiometry, confirmed by XRD (Table 1) and initial SEM-EDS screening of polished UOC mounts. This uranium heterogeneity manifests in complex relationships with other elements. For instance, in the bench-scale UO_4 sample, high-uranium phases (identified by highest BSE brightness) coincide with elevated sulfur concentrations (Fig. 8). Conversely, in the commercial ADU particle, high-uranium phases show no correlation with other analyzed elements (Fig. 6). These observations indicate that a single UOC particle contains multiple uranium compounds, a complexity that bulk XRD characterization of UOC powders may obscure. Techniques with higher spatial resolution, such as micro-XRD and micro-Raman, would likely provide more accurate characterization of these compositionally diverse materials **[28]**.

A major finding of this study is that commercial UOC particles are substantially more heterogeneous than bench-scale UOC particles in our dataset. This is evident in PCA space, where commercial UOCs display a much larger spread along PC1 and PC2 compared to the bench-scale samples (Fig. 11). The separation between the commercial UOCs is driven primarily by variations in S, Ca, Ti, and Na content, with Ca and S dominating variability in commercial ADU and Ti and Na in commercial $UO_4 \bullet 4H_2O$. These elemental patterns can be correlated to specific processing methods; for example, high S in commercial ADU results from sulfuric acid and ammonium sulfate use, while elevated Na in commercial $UO_4 \bullet 4H_2O$ is linked to sodium carbonate used as a process chemical during ion-exchange. At industrial production scales, these chemical impurities are not uniformly distributed within (Figs. 6–7) and among all particles (Figs. S4–S5), which contributes to the great heterogeneity of the commercial samples. Overall, the PCA

results show that spatially correlated elemental compositions not only distinguish the two commercial UOCs from each other and from the bench-scale samples in this study but also could be used to differentiate commercial and bench-scale UO_4 materials from other production streams.

Compositional differences between the two bench-scale samples are subtle; both overlap in PC1 versus PC2 space, with distinctions only evident in PC3 versus PC 4 space (Fig. 11). This similarity is expected, as the bench-scale UO_2 was produced directly from the bench-scale UO_4. Variability in bench-scale UO_4 is primarily influenced by S, whereas variability in UO_2 is driven by Na and Mo. The bench-scale UO_2 also contains localized enrichments in Ti, Mo, Cr, and Fe ranging from a few weight percent to 25 wt. %, particularly within accreted conglomerate phases in some particles (Figs. 5 and S4). Notably, not all bench-scale UO_2 particles show the metal impurities. These trace metals were likely introduced as contaminants during calcination, which was performed in a Hastelloy reactor—a potential source of Cr, Fe, and Mo through corrosion (Fig. S4). The presence of several weight percent Mo in 7% of the bench-scale UO_4 analyses indicates that some impurities predate calcination, likely inherited from the source uranium used in bench-scale production. Sulfur- and sodiu- rich phases present in the bench-scale UO_4 particles are not observed in the calcined UO_2 particles. This suggests that the calcination process either redistributes these chemical impurities or migrates them into portions of the oxide that were not analyzed. Overall, the calcination process produces partial chemical homogenization but also introduces metal contaminants.

What can particle cross-sections tell us about calcination?

The effects of calcination on UOCs can be further evaluated by examining the BSE cross-sectional particle images of the bench-scale UOCs to assess how particle phases change before and after this process (Figs. 4–5). In the pre-calcined UO_4 particles, inclusions and high-sulfur phases are present. Aside from the accreted conglomerate phase, the post-calcined bench-scale UO_2 consists of a groundmass matrix, high-uranium phase and a crystal-lath phase. There are no clear elemental differences between the bench-scale UO_2 phases based on the elements analyzed suggesting the phases represent

different uranium compounds. Previous ADU calcination experiments demonstrated that the final calcined product typically consists of a mixture of two uranium oxide particles, based on stoichiometry [44]. Our study builds on this understanding by demonstrating that impurities are heterogeneously distributed among different uranium compounds (Table 1) in a single UOC particle, a trend not detectable through bulk analysis of UOC.

The crystal laths phase in the bench-scale UO_2 is particularly interesting because they resemble acicular (needle-like or lath-like) plagioclase crystals found in some basaltic rocks [45, 46]. Basaltic magmas typically have temperatures between 1000 and 1200 °C. As the magma cools, it passes through the equilibrium crystallization temperature, where solid crystals begin to nucleate and grow. In some cases, rapid cooling causes the magma to drop well below this temperature boundary, leading to supercooling—a process in which nucleation begins at significantly lower temperatures (~50–200 °C below the equilibrium crystallization temperature) [47–49]. Supercooling results in rapid and extensive nucleation but limited crystal growth, producing abundant long, acicular or lath-like crystals. While the calcination of UOC does not involve melting, the formation of lath-like crystals suggests that rapid sub-solidus recrystallization might have occurred, analogous to the way rapid cooling in basaltic magmas produces acicular crystals. This analogy suggests that faster cooling rates can promote the development of acicular phase morphologies in UOC, even though the underlying mechanisms differ. The bench-scale UO_2 was calcined at 550 °C for seven hours in a small, lab-scale Hastelloy vessel. Smaller vessels cool more quickly, and rapid cooling can promote the formation of metastable, elongated phase morphologies rather than the more stable blocky or tabular morphologies typically seen with slower cooling. Thus, the lath textures in the bench-scale UO_2 might provide insight into the cooling rate of the calcination process.

Connecting microscale and bulk-scale elemental characteristics

A clear understanding of how microscale impurity concentrations and distributions in individual UOC particles correspond to bulk scale impurity measurements is crucial for the effective use of microanalytical techniques and for interpreting nuclear forensic results, especially when sample quantities are limited. [28, 31, 50]. This relationship

works both ways: it's essential to understand the scale at which the microscale features accurately represent bulk properties, while also recognizing that microscale features reflect unique and diagnostic characteristics that are not apparent in analysis of material at a bulk scale.

Fig. 12 Comparison of elemental concentrations in commercial UOCs measured by EPMA (boxes) and ICP-MS (circles), reported in µg/g. The commercial ADU sample is shown as gray boxes and black circles, and the commercial UO_4 sample as blue boxes and blue circles. EPMA box plots include only measurements above the detection limit. ICP-MS values represent the mean of four independent bulk digestions, each analyzed in triplicate

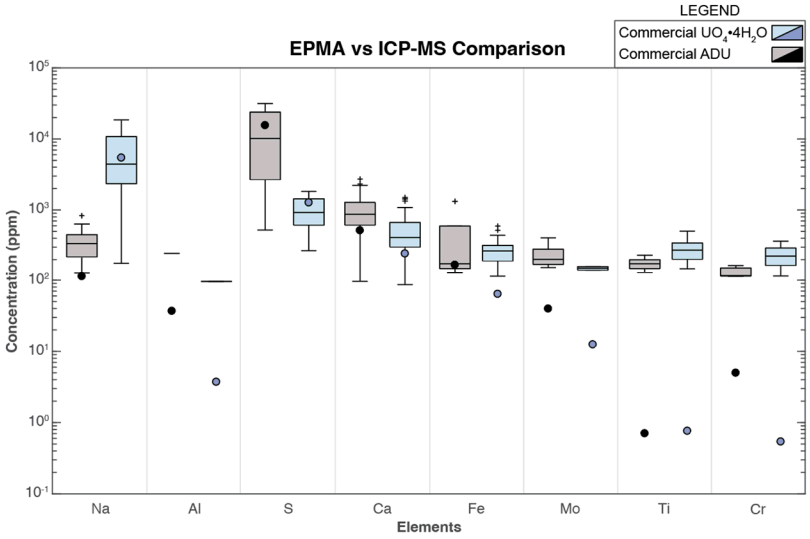

To evaluate the relationship between microscale and bulk compositions, we compared elemental data obtained by EPMA with bulk analyses of commercial UOC samples measured by ICP-MS (Supplementary Table 3). Our results demonstrate a strong correlation between EPMA and ICP-MS concentrations for elements present above several hundred ppm, such as S, Ca, and Na (Fig. 12). For transition metals, however, EPMA values are consistently higher than bulk measurements. This discrepancy is primarily due to the concentration of these elements in minor phases within UOC particles, as well as potential selection bias toward texturally distinct regions in BSE imagery. The correlation further weakens for elements near the EPMA detection limits, such as Al, Ti, and Cr, where EPMA cannot reliably represent bulk compositions. Nevertheless, EPMA remains a powerful tool for detecting trace impurities that may be

missed by bulk ICP-MS analyses. Importantly, even when absolute concentrations differ, EPMA reliably captures relative compositional differences between samples. These findings validate EPMA as a valuable tool for inferring bulk composition from particle analyses and demonstrate its utility in correlating single-particle data with bulk-scale compositional characteristics of UOCs, indicating the utility of this analytical approach for nuclear forensics even when sample material is limited.

Using EPMA as a nuclear forensics tool

Electron microprobes are powerful tools for documenting microscale impurities and chemical heterogeneities within UOC particles because it is purpose-built for quantitative trace-element microanalysis. EPMA couples a highly stable, well-controlled electron beam with standards-based WDS, providing fully quantitative concentrations and enabling long (2–3 h) mapping runs under stable beam conditions. For WDS, trace performance is fundamentally count-statistics limited: detection limit is inversely proportional to the square root of peak/background ratio, background-corrected on-peak count rate, and counting time, so trace-element work commonly requires increased count time and/or beam current [51]. Dedicated microprobes also reduce analysis time for trace mapping by counting an element on multiple WDS spectrometers and aggregating counts, supporting detection limits in the tens of ppm range in favorable cases, with best-case performance reported around ~ 1 ppm with specialize techniques [52]. By contrast, even when peak overlap is not significant, SEM-EDS trace sensitivity typically requires long acquisitions and still tends to be limited to the few-hundred-ppm range (e.g., ~200–500 ppm achievable with counting times below ~500 s) [53]. While some SEMs can be equipped with WDS, WDS spectra are acquired sequentially and SEM-WDS configurations often provide fewer parallel WDS channels than a dedicated EPMA, making multi-element trace mapping comparatively time-prohibitive [51].

Several important considerations arise when applying EPMA to UOC particles. Accurate analysis requires meticulous sample preparation, specifically creating smooth, polished surfaces. Mounting UOC powders in epoxy is the simplest method, but it tends to favor larger particles, with smaller particles potentially lost during polishing. For

limited or very small samples, individual particles can be mounted on silicon or carbon planchettes and polished using ion-etching techniques like focused ion beam milling [54].

Another important consideration is the use of formula-by-difference method for calculating EPMA concentrations presents certain limitations. This approach requires prior knowledge of UOC stoichiometry, which must be independently determined (e.g., by X-ray diffraction, see Table 1). The method assumes stoichiometric homogeneity across all phases and particles, an assumption that may not always hold true. Additionally, normalizing concentrations to 100% can skew results if not all major constituents are measured, potentially overlooking unmeasured elements. In this study, we balanced analysis time, element selection, and counting time when determining which elements to include in spot analyses and quantitative maps. We prioritized measuring elements likely to exist as impurities in the UOC samples while excluding nitrogen, oxygen, silicon, and carbon, despite their significance as major or potential major constituents. Nevertheless, characterizing impurity distribution patterns in UOC samples remains important for understanding the processing histories of these early fuel cycle materials.

Conclusions

Microscale heterogeneities in UOCs are diagnostic of both provenance and processing methods. The spatial scale of heterogeneity is on the order of several microns, with polydisperse particles including multiple phases with contrasting morphologies, composition, and stoichiometries. High-resolution EPMA imagery and quantitative analyses show that chemical impurities are heterogeneously distributed within individual particles and among particles in a sample.

Microscale characteristics can be directly linked to processing conditions. In the bench-scale UO_2 particles, enrichment in Cr, Fe, and other trace elements is attributed to interaction with the Hastelloy reactor, while acicular, crystal lath phases may reflect rapid cooling during calcination. In the commercial UOC samples, high-sulfur phases in ADU particles result from the use of sulfuric acid and ammonium sulfate, and elevated Na in $UO_4•4H_2O$ is associated with sodium carbonate used during ion exchange. Commercial

UOCs exhibit greater overall heterogeneity, indicating that plant-scale operations do not fully homogenize material prior to or during precipitation. In contrast, the paired bench-scale UOC samples are largely indistinguishable, aside from minor metal contamination introduced during post-calcination processing.

Comparisons between EPMA spot analyses and bulk ICP-MS compositions show that EPMA can reliably approximate bulk compositions for elements at high concentrations (greater than 500 ppm). EPMA is also more sensitive to some trace impurities, such as transition metals, that may be obscured in bulk ICP-MS data. Together, these results indicate that (1) microscale impurities observed in-situ can be lost or averaged out in bulk analyses, and (2) bulk UOC compositions can be extrapolated from EPMA spot analyses for major and high concentration minor elements, which is particularly valuable when sample quantities are limited.

Overall, this study demonstrates the utility of microscale signatures in early fuel cycle materials for nuclear forensic investigations.

Acknowledgements

This research was supported in part by the Department of Homeland Security's National Nuclear Forensic Expertise Development Program Postdoctoral Fellowship. We gratefully acknowledge Paul Taylor and his team at Oak Ridge National Laboratory for preparing and providing the bench-scale UOC samples used in this study. We also thank Christina Ramon and Danielle (Ziva) Shulaker for their guidance in sample preparation, and Sarah Roberts for XRD analysis of the commercial UOCs. This work was performed under the auspices of the U.S. Department of Energy by Lawrence Livermore National Laboratory. LLNL-JRNL-2014890.

References

1. Keegan E, Kristo MJ, Toole K, et al (2016) Nuclear Forensics: Scientific Analysis Supporting Law Enforcement and Nuclear Security Investigations. Anal Chem 88:1496–1505. https://doi.org/10.1021/acs.analchem.5b02915

2. Mayer K, Wallenius M, Varga Z (2013) Nuclear Forensic Science: Correlating Measurable Material Parameters to the History of Nuclear Material. Chem Rev 113:884–900. https://doi.org/10.1021/cr300273f

3. Kristo MJ, Gaffney AM, Marks N, et al (2016) Nuclear Forensic Science: Analysis of Nuclear Material Out of Regulatory Control. Annu Rev Earth Planet Sci 44:555–579. https://doi.org/10.1146/annurev-earth-060115-012309

4. Reed SJB (2005) Electron Microprobe Analysis and Scanning Electron Microscopy in Geology, 2nd ed. Cambridge University Press

5. Rinaldi R, Llovet X (2015) Electron Probe Microanalysis: A Review of the Past, Present, and Future. Microsc Microanal 21:1053–1069. https://doi.org/10.1017/S1431927615000409

6. Sharp N, McDonough WF, Ticknor BW, et al (2014) Rapid analysis of trinitite with nuclear forensic applications for post-detonation material analyses. J Radioanal Nucl Chem 302:57–67. https://doi.org/10.1007/s10967-014-3285-9

7. Boro J, Marks N, Luitjohan K (2024) Multi-Point or Mean Atomic Number Backgrounds? Trace Element Quantification of Intentionally Tagged U Fuels Using EPMA. Microscopy and Microanalysis 30:ozae044.621. https://doi.org/10.1093/mam/ozae044.621

8. Riche AT, McSwiggen P, Harvey K, et al (2025) Mixed Element Microparticle Characterization by Electron Probe Microanalysis. Microscopy and Microanalysis 31:ozaf022. https://doi.org/10.1093/mam/ozaf022

9. Keegan E, Richter S, Kelly I, et al (2008) The provenance of Australian uranium ore concentrates by elemental and isotopic analysis. Applied Geochemistry 23:765–777. https://doi.org/10.1016/j.apgeochem.2007.12.004

10. Švedkauskaitė-LeGore J, Rasmussen G, Abousahl S, van Belle P (2008) Investigation of the sample characteristics needed for the determination of the origin of uranium-bearing materials. J Radioanal Nucl Chem 278:201–209. https://doi.org/10.1007/s10967-007-7215-y

11. Varga Z, Wallenius M, Mayer K (2010) Origin assessment of uranium ore concentrates based on their rare-earth elemental impurity pattern. Radiochimica Acta 98:771–778. https://doi.org/10.1524/ract.2010.1777

12. Keegan E, Wallenius M, Mayer K, et al (2012) Attribution of uranium ore concentrates using elemental and anionic data. Applied Geochemistry 27:1600–1609. https://doi.org/10.1016/j.apgeochem.2012.05.009

13. Lin M, Zhao Y, Zhao L, et al (2015) Tracing origins of uranium ore concentrates (UOCs) by multidimensional statistical analysis of rare-earth impurities. Journal of Analytical Atomic Spectrometry 30:396–402. https://doi.org/10.1039/C4JA00354C

14. Varga Z, Krajkó J, Peńkin M, et al (2017) Identification of uranium signatures relevant for nuclear safeguards and forensics. J Radioanal Nucl Chem 312:639–654. https://doi.org/10.1007/s10967-017-5247-5

15. El Haddad J, Harhira A, Blouin A, et al (2018) Discrimination of uranium ore concentrates by chemometric data analysis to support provenance assessment for nuclear forensics applications. J Radioanal Nucl Chem 317:625–632. https://doi.org/10.1007/s10967-018-5912-3

16. Fletcher ND, Manard BT, Bostick DA, et al (2021) Determination of phosphorus and sulfur in uranium ore concentrates by triple quadrupole inductively coupled plasma mass spectrometry. Talanta 221:121573. https://doi.org/10.1016/j.talanta.2020.121573

17. Spano TL, Simonetti A, Balboni E, et al (2017) Trace element and U isotope analysis of uraninite and ore concentrate: Applications for nuclear forensic investigations. Applied Geochemistry 84:277–285. https://doi.org/10.1016/j.apgeochem.2017.07.003

18. Varga Z, Wallenius M, Mayer K, Meppen M (2011) Analysis of uranium ore concentrates for origin assessment. Proceedings in Radiochemistry 1:27–30. https://doi.org/10.1524/rcpr.2011.0004

19. Varga Z, Wallenius M, Mayer K, et al (2009) Application of Lead and Strontium Isotope Ratio Measurements for the Origin Assessment of Uranium Ore Concentrates. Anal Chem 81:8327–8334. https://doi.org/10.1021/ac901100e

20. Krajkó J, Varga Z, Wallenius M, et al (2016) Investigation of sulphur isotope variation due to different processes applied during uranium ore concentrate production. J Radioanal Nucl Chem 309:1113–1121. https://doi.org/10.1007/s10967-016-4733-5

21. Rolison JM, Druce M, Shollenberger QR, et al (2019) Molybdenum isotope compositions of uranium ore concentrates by double spike MC-ICP-MS. Applied Geochemistry 103:97–105. https://doi.org/10.1016/j.apgeochem.2019.03.001

22. Brennecka GA, Borg LE, Hutcheon ID, et al (2010) Natural variations in uranium isotope ratios of uranium ore concentrates: Understanding the 238U/235U fractionation mechanism. Earth and Planetary Science Letters 291:228–233. https://doi.org/10.1016/j.epsl.2010.01.023

23. Devlin McLoughlin VE, Shollenberger QR, Brennecka GA (2023) Determining provenance of uranium ore concentrates using 143Nd/144Nd. Talanta 253:124088. https://doi.org/10.1016/j.talanta.2022.124088

24. Uvarova YA, Kyser TK, Geagea ML, Chipley D (2014) Variations in the uranium isotopic compositions of uranium ores from different types of uranium deposits.

Geochimica et Cosmochimica Acta 146:1–17. https://doi.org/10.1016/j.gca.2014.09.034

25. Kips R, Leenaers A, Tamborini G, et al (2007) Characterization of Uranium Particles Produced by Hydrolysis of UF_6 Using SEM and SIMS. Microsc Microanal 13:156–164. https://doi.org/10.1017/S1431927607070341

26. Ranebo Y, Eriksson M, Tamborini G, et al (2007) The Use of SIMS and SEM for the Characterization of Individual Particles with a Matrix Originating from a Nuclear Weapon. Microsc Microanal 13:179–190. https://doi.org/10.1017/S1431927607070353

27. Chen Y, Shen Y, Chang Z-Y, et al (2013) Studies on analyzing single uranium-bearing particle by FT-TIMS. Radiation Measurements 50:43–45. https://doi.org/10.1016/j.radmeas.2012.10.015

28. Crean DE, Corkhill CL, Nicholls T, et al (2015) Expanding the nuclear forensic toolkit: chemical profiling of uranium ore concentrate particles by synchrotron X-ray microanalysis. RSC Adv 5:87908–87918. https://doi.org/10.1039/C5RA14963K

29. Donard A, Pointurier F, Pottin A-C, et al (2017) Determination of the isotopic composition of micrometric uranium particles by UV femtosecond laser ablation coupled with sector-field single-collector ICP-MS. Journal of Analytical Atomic Spectrometry 32:96–106. https://doi.org/10.1039/C6JA00071A

30. Tamasi AL, Cash LJ, Mullen WT, et al (2017) Morphology of U3O8 materials following storage under controlled conditions of temperature and relative humidity. J Radioanal Nucl Chem 311:35–42. https://doi.org/10.1007/s10967-016-4923-1

31. Pointurier F, Ho Mer Lin D, Manara D, et al (2019) Capabilities of micro-Raman spectrometry for the identification of uranium ore concentrates from analysis of single particles. Vibrational Spectroscopy 103:102925. https://doi.org/10.1016/j.vibspec.2019.05.007

32. Strashnov I, Izosimov I, D. Gilmour J, et al (2019) A laser ablation resonance ionisation mass spectrometer (LA-RIMS) for the detection of isotope ratios of uranium at ultra-trace concentrations from solid particles and solutions. Journal of Analytical Atomic Spectrometry 34:1630–1638. https://doi.org/10.1039/C9JA00030E

33. Wimpenny J, Samperton KM, Sotorrio P, et al (2023) Rapid isotopic analysis of uranium particles by laser ablation MC-ICP-MS. J Anal At Spectrom 38:827–840. https://doi.org/10.1039/D2JA00403H

34. Nielsen CH, Sigurdsson H (1981) Quantitative methods for electron microprobe analysis of sodium in natural and synthetic glasses. American Mineralogist 66:547–552

35. Morgan GB, London D (1996) Optimizing the electron microprobe analysis of hydrous alkali aluminosilicate glasses. American Mineralogist 81:1176–1185. https://doi.org/10.2138/am-1996-9-1016

36. Donovan JJ, Tingle TN (1996) An Improved Mean Atomic Number Background Correction for Quantitative Microanalysis. Microsc Microanal 2:1–7. https://doi.org/10.1017/S1431927696210013

37. Donovan JJ, Singer JW, Armstrong JT (2016) A new EPMA method for fast trace element analysis in simple matrices. American Mineralogist 101:1839–1853. https://doi.org/10.2138/am-2016-5628

38. Donovan JJ, Allaz JM, Handt A von der, et al (2021) Quantitative WDS compositional mapping using the electron microprobe. American Mineralogist 106:1717–1735. https://doi.org/10.2138/am-2021-7739

39. Tamasi AL, Cash LJ, Eley C, et al (2016) A lexicon for consistent description of material images for nuclear forensics. J Radioanal Nucl Chem 307:1611–1619. https://doi.org/10.1007/s10967-015-4455-0

40. Reimann C, Filzmoser P, Garrett RG, Dutter R (2008) Statistical Data Analysis Explained: Applied Environmental Statistics with R, 1st ed. Wiley

41. Olsen AM, Richards B, Schwerdt I, et al (2017) Quantifying Morphological Features of α-U_3 O_8 with Image Analysis for Nuclear Forensics. Anal Chem 89:3177–3183. https://doi.org/10.1021/acs.analchem.6b05020

42. Ly C, Olsen AM, Schwerdt IJ, et al (2019) A new approach for quantifying morphological features of U3O8 for nuclear forensics using a deep learning model. Journal of Nuclear Materials 517:128–137. https://doi.org/10.1016/j.jnucmat.2019.01.042

43. Said M, Marks NE, Dai Z, Lindvall RE (2022) Qualitative assessment of uranium ore concentrates and related materials using scanning electron microscopy. J Radioanal Nucl Chem 331:5053–5060. https://doi.org/10.1007/s10967-022-08605-6

44. Manna S, Roy SB, Joshi JB (2012) Study of crystallization and morphology of ammonium diuranate and uranium oxide. Journal of Nuclear Materials 424:94–100. https://doi.org/10.1016/j.jnucmat.2012.02.012

45. Winter JD (2014) Principles of igneous and metamorphic petrology, 2. ed., Pearson new internat. ed. Pearson Education, Harlow

46. Philpotts AR, Ague JJ (2022) Principles of Igneous and Metamorphic Petrology, 3rd ed. Cambridge University Press

47. Lofgren G (1974) An experimental study of plagioclase crystal morphology; isothermal crystallization. American Journal of Science 274:243–273. https://doi.org/10.2475/ajs.274.3.243

48. Donaldson CH (1976) An experimental investigation of olivine morphology. Contr Mineral and Petrol 57:187–213. https://doi.org/10.1007/BF00405225

49. Cashman KV (1993) Relationship between plagioclase crystallization and cooling rate in basaltic melts. Contr Mineral and Petrol 113:126–142. https://doi.org/10.1007/BF00320836

50. McDonald LW, Sentz K, Hagen A, et al (2024) Review of multi-faceted morphologic signatures of actinide process materials for nuclear forensic science. Journal of Nuclear Materials 588:154779. https://doi.org/10.1016/j.jnucmat.2023.154779

51. Walshaw RD (2018) Electron probe microanalysis (EPMA) in the Earth Sciences. University of Bristol, University of Bristol, pp 77–92

52. Boro JR, Wolff JA, Neill OK, et al (2021) Titanium diffusion profiles and melt inclusion chemistry and morphology in quartz from the Tshirege Member of the Bandelier Tuff. American Mineralogist 106:620–632. https://doi.org/10.2138/am-2021-7395

53. Newbury DE, Ritchie NWM (2019) Electron-Excited X-ray Microanalysis by Energy Dispersive Spectrometry at 50: Analytical Accuracy, Precision, Trace Sensitivity, and Quantitative Compositional Mapping. Microsc Microanal 25:1075–1105. https://doi.org/10.1017/S143192761901482X

54. Reilly DD, Beck CL, Buck EC, et al (2020) Focused ion beam for improved spatially-resolved mass spectrometry and analysis of radioactive materials for uranium isotopic analysis. Talanta 211:120720. https://doi.org/10.1016/j.talanta.2020.120720